# Complexity of the laminar-turbulent boundary in pipe flow

Nazmi Burak Budanur[1,2,*] and Björn Hof[1]

[1]*Nonlinear Dynamics and Turbulence Group, IST Austria, 3400 Klosterneuburg, Austria*
[2]*Kavli Institute for Theoretical Physics, UC Santa Barbara, Santa Barbara, California 93106, USA*

Over the past decade, the edge of chaos has proven to be a fruitful starting point for investigations of shear flows when the laminar base flow is linearly stable. Numerous computational studies of shear flows demonstrated the existence of states that separate laminar and turbulent regions of the state space. In addition, some studies determined invariant solutions that reside on this edge. In this paper, we study the unstable manifold of one such solution with the aid of continuous symmetry reduction, which we formulate here for the simultaneous quotiening of axial and azimuthal symmetries. Upon our investigation of the unstable manifold, we discover a previously unknown traveling-wave solution on the laminar-turbulent boundary with a relatively complex structure. By means of low-dimensional projections, we visualize different dynamical paths that connect these solutions to the turbulence. Our numerical experiments demonstrate that the laminar-turbulent boundary exhibits qualitatively different regions whose properties are influenced by the nearby invariant solutions.

## I. INTRODUCTION

Pipe flow is the most prominent member of a class of canonical shear flows where a transition to turbulence occurs despite the linear stability of the laminar state [1]. In the past two decades this problem has enjoyed several major developments. The discovery of nonlinear traveling-wave solutions [2–4] and studies [5–7] of the laminar-turbulent boundary began to elucidate the state space of the system using insights from dynamical systems theory.

In the dynamical system approach to turbulence, fluid motion is envisioned as a trajectory in an infinite-dimensional state space [8]. For the case of shear flows with linearly stable laminar solutions, this state space accommodates a stable equilibrium point corresponding to the laminar solution and a chaotic set (an attractor or repeller) that is turbulent. Once this viewpoint is established, a natural question to ask is what separates these two distinct regions in the state space. In a small computational cell of channel flow, Itano and Toh [9] studied solutions that neither laminarize nor become turbulent using a shooting method and they discovered that such trajectories tend towards a traveling-wave solution. Following studies of shear flows in similar computational domains found periodiclike [10], equilibrium [11], and seemingly chaotic [5] solutions using similar shooting methods. These findings suggested the following picture of the state space of shear flows: The basin boundary between laminar and turbulent solutions is the stable manifold of an invariant set, whose unstable manifold connects on one side to the laminar solution and on the other side to the turbulent part of the state space. Schneider *et al.* [5] named this invariant set the edge state.

Schneider *et al.* [5] found in a short axially periodic computational domain of pipe flow that the edge state exhibits chaotic motion, with flow structures much simpler than those of turbulence: a slow streak in the center surrounded by two fast streaks with chaotically moving streamwise vortices in

---

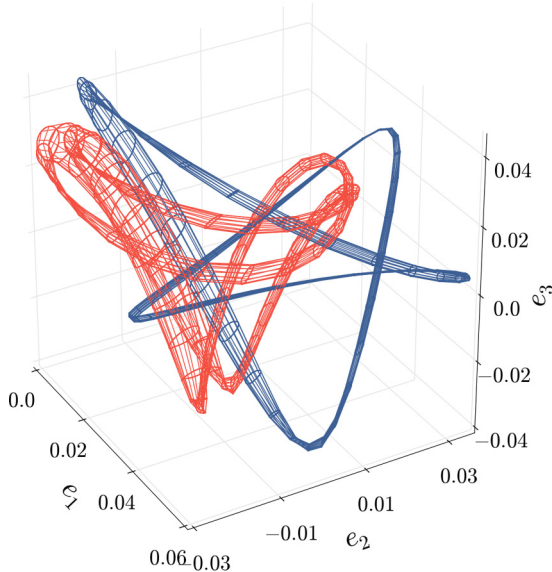*Corresponding author: burak.budanur@ist.ac.at

FIG. 1. Two traveling-wave solutions of pipe flow (S1 and S1N, to be described later in the article) and their continuum of symmetry copies obtained from the axial translations and the azimuthal rotations, visualized as red and blue wire frames projected from the state space. Projection bases are the same as in Figs. 4 and 5. Apparent intersections of the curves are the artifacts of finite-dimensional projection from the infinite-dimensional state space. In the symmetry-reduced state space, each torus will be represented by a single point.

between. A similar investigation in a long computational domain of pipe flow [7] yielded streamwise localized edge states with chaotic dynamics, whose flow fields at the core of the localized structure resembled those computed in the short computational domain.

Typically when flows are not simplified by additional symmetries the edge state tends to be chaotic, as is the case for plane Couette [12], channel [13], and asymptotic suction boundary-layer [14] flows. In this seemingly generic case, the definition of the edge state is less clear than when it is formed by an exact invariant solution such as a (relative) equilibrium or a (relative) periodic orbit. In contrast to the invariant solutions, it is not straightforward to define and compute the stable and unstable manifolds of chaotic solutions, hence their theoretical study is much more challenging.

One way of systematically investigating chaotic edge states is by studying the unstable invariant solutions that are contained within, since the geometry of chaotic sets are influenced by the invariant solutions that are embedded in them [15]. This strategy was adopted by Duguet *et al.* [6], who found for the case of pipe flow in an approximately five-diameter-long axially periodic computational domain at Re = 2875 (Re based on bulk velocity and pipe diameter) that the chaotic edge state evolves around the asymmetric traveling-wave solution found by Pringle and Kerswell [3]. In addition, they found a rotating traveling wave that had flow structures very similar to those of the asymmetric wave, but differently it rotated in the azimuthal direction in addition to drifting downstream.

Canonical shear flows (pipe, plane Couette, and plane Poiseuille) are symmetric under continuous translations in streamwise and spanwise (or azimuthal, in the case of pipe flow) directions. This implies that every generic (nonsymmetric) solution of these systems has infinitely many copies that can be generated by symmetry transformations. We visualized this degeneracy in Fig. 1 for two traveling-wave solutions we study in this article. Due to this multiplicity, something as simple as measuring the distance between two solutions becomes a daunting task. As a result, a common practice in the dynamical system approach to turbulence literature is to use quantities averaged over computational domains, such as energy input, dissipation, or pressure gradient, as indicators of closeness in the state space [14,16–18]. While observing such quantities can be used for deciding

if two solutions are far from each other, they cannot be used to conclusively decide if two solutions are close in the state space: Two solutions that have similar rates of energy input, dissipation, and pressure drop might have completely different flow structures. In this paper, this problem is addressed by symmetry reduction in both axial and azimuthal directions of pipe flow. In the symmetry-reduced state space, the tori, such as those visualized in Fig. 1, are represented by single points, which simplifies the analysis substantially. As we will explain later in the article, our approach to this problem is generic and adaptable to other canonical shear flow geometries in a straightforward fashion.

For the application of our methods, we chose to revisit the laminar-turbulent boundary in a short (approximately five diameters) pipe flow at Re = 3000. To this end, we visualize numerical approximations to the unstable manifold of the asymmetric traveling wave that reside in the laminar-turbulent boundary on local projections akin to those pioneered by Gibson *et al.* [19]. We demonstrate that some parts of this unstable manifold that belong to the laminar-turbulent boundary exhibit dynamics qualitatively different from those previously attributed to the edge state in this setting. Upon further investigation, we discover that this region is in the vicinity of a traveling-wave solution with four high-speed streamwise streaks. This traveling wave appears to belong to a higher-energy region in the edge state, closer to the turbulent part of the state space. We study the unstable manifold of this traveling wave and demonstrate its different connections to the turbulence. Finally, we present the results of numerical experiments, which demonstrate that the trajectories on the laminar-turbulent boundary of pipe flow transiently approach the traveling waves that reside in the edge.

The rest of the paper is organized as follows. In the next section, we overview our methods; particularly in Sec. II D, we present the generalization of the first Fourier mode slice [20] for simultaneous reduction of continuous symmetries in the axial and azimuthal directions. We present our results in Sec. III, followed by a summary and discussion in Sec. IV.

## II. METHODS

### A. Numerical setup

Numerical integration of the Navier-Stokes equations

$$\mathbf{u}_\tau + \mathbf{u}_{\mathrm{HP}} \cdot \nabla \mathbf{u} + \mathbf{u} \cdot \nabla \mathbf{u}_{\mathrm{HP}} + \mathbf{u} \cdot \nabla \mathbf{u} = -\nabla p + 32 \frac{\beta}{\mathrm{Re}} \hat{\mathbf{z}} + \frac{1}{\mathrm{Re}} \nabla^2 \mathbf{u} \qquad (1)$$

are performed using Openpipeflow [21]. The velocity field $\mathbf{u}(z,r,\theta;\tau)$ denotes the deviations from the base (Hagen-Poiseuille) solution $\mathbf{u}_{\mathrm{HP}}(z,r,\theta) = 2[1 - (2r)^2]\hat{\mathbf{z}}$. Lengths and velocities are nondimensionalized by the pipe diameter $D$ and the mean axial speed $U$. Boundary conditions are no slip and impermeable on pipe walls $\mathbf{u}(r = 1/2) = 0$ and periodic in the axial and azimuthal directions $\mathbf{u}(z,r,\theta) = \mathbf{u}(z + kL, r, \theta + m2\pi)$, $k,m \in \mathbb{Z}$. The velocity field satisfies the incompressibility condition $\nabla \cdot \mathbf{u} = 0$ and $\beta = \beta[\mathbf{u}(\tau)]$ is a feedback term, adjusted in order to ensure a constant flux equal to that of the laminar solution at a given Re. For all results of this paper, Re = $UD/\nu$ = 3000; the pipe length is set to $L = \pi/0.625 \approx 5$; flow fields are discretized using $N = 128$ finite-difference points in the radial direction and a Fourier series truncated at $K = M = 64$ in the axial and azimuthal directions, respectively. Nonlinear terms are evaluated in the physical space on $N \times 3K \times 3M$ grid points following the 3/2 rule for dealiasing in Fourier-expanded directions. This truncation yields more than $6 \times 10^6$ numerical degrees of freedom, which is significantly higher than the typical resolutions used in similar computational studies [5,22]. Our choice yields an at least five orders of magnitude drop in the spectral coefficients of the turbulent solutions at Re = 3000. While the solutions in the edge state generally require much fewer degrees of freedom to be resolved, we made this "conservative" choice since we investigate different regions of the edge state and we did not know *a priori* the maximum resolution requirement.

## B. Symmetries

In this section, we review the symmetries of pipe flow and their representations in terms of their actions on the velocity field. For more detailed discussions of the symmetries and the invariant subspaces of pipe flow, we refer the reader to Refs. [23,24]. Pipe flow is equivariant under the axial translations $g_z(l)$, $l \in [0,L)$, the azimuthal rotations $g_\theta(\phi)$ $\phi \in [0,2\pi)$, and the reflection $\sigma$, whose actions on the axial $u$, radial $v$, and azimuthal $w$ components of the velocity field are given by

$$g_z(l)[u,v,w](z,r,\theta) = [u,v,w](z-l,r,\theta), \tag{2}$$

$$g_\theta(\phi)[u,v,w](z,r,\theta) = [u,v,w](z,r,\theta-\phi), \tag{3}$$

$$\sigma[u,v,w](z,r,\theta) = [u,v,-w](z,r,-\theta). \tag{4}$$

Therefore, the symmetry group of pipe flow is the direct product of $\mathrm{SO}(2)_z$ and $\mathrm{O}(2)_\theta$, i.e.,

$$G = \mathrm{SO}(2)_z \times \mathrm{O}(2)_\theta = \{g_z(l), g_\theta(\phi), \sigma\}. \tag{5}$$

Lie group actions (2) and (3) can be written as operator exponentials of their respective infinitesimal generators $T_z$ and $T_\theta$ as

$$g_z(l) = e^{T_z l}, \quad g_\theta(\phi) = e^{T_\theta \phi}, \tag{6}$$

where the actions of $T_z$ and $T_\theta$ on the velocity field $\mathbf{u} = \mathbf{u}(z,r,\theta)$ are

$$T_z \mathbf{u} = -\frac{\partial}{\partial z}\mathbf{u}, \quad T_\theta \mathbf{u} = -\frac{\partial}{\partial \theta}\mathbf{u}. \tag{7}$$

## C. State-space notation

Since we are going to use dynamical systems tools, it is handy to introduce state-space notation for use in the rest of the paper. Let $a(0)$ be a vector that contains all numerical degrees of freedom of a three-dimensional velocity field $\mathbf{u}(z,r,\theta;0)$ at an initial time $\tau = 0$. Then the Navier-Stokes equations (1) along with the incompressibility and the boundary conditions imply a finite-time flow

$$a(\tau) = f^\tau(a(0)), \tag{8}$$

where $a(\tau)$ corresponds to the velocity field $\mathbf{u}(z,r,\theta;\tau)$ at time $\tau$. Assuming that the flow (8) is smooth, we can also represent the system as a high-dimensional ordinary differential equation

$$\dot{a} = v(a) = \lim_{\delta\tau \to 0}[f^{\delta\tau}(a) - a]/\delta\tau. \tag{9}$$

Actions of group elements $g \in G$ on a state space vector $a$ should be thought of as actions on the corresponding velocity fields as in (2)–(4). In other words, if $a$ corresponds to the velocity field $\mathbf{u}$ then $ga$ corresponds to the transformed velocity field $g\mathbf{u}$. Similarly, group tangents $t_{z,\theta}(a) = T_{z,\theta}a$ correspond to velocity fields $T_{z,\theta}\mathbf{u}$, where $T_{z,\theta}$ acts as in (7). In the state space, equivariance under $g$ implies that the state-space velocity and finite-time flow commute with $g$, i.e.,

$$v(ga) = gv(a), \quad f^\tau(ga) = gf^\tau(a). \tag{10}$$

Letting $a$ and $a'$ correspond to velocity fields $\mathbf{u}$ and $\mathbf{u}'$, respectively, we define the inner product

$$\langle a,a' \rangle = \frac{1}{2}\int \mathbf{u} \cdot \mathbf{u}' dV, \tag{11}$$

where the integral is carried over the pipe volume. Thus, $\|a\|^2 = \langle a,a \rangle$ gives the kinetic energy of the velocity fluctuations; hence this choice of norm is usually referred to as the energy norm.

### D. Continuous-symmetry reduction

We define the group orbit $\mathcal{M}_a$ of a state-space point $a$ as all points reachable from $a$ by symmetry transformations, i.e.,

$$\mathcal{M}_a = \{ga \mid g \in G\}. \tag{12}$$

If $a$ is not invariant under any symmetries of the system, its group orbit (12) defines two distinct 2-tori that are related to each other by the reflection $\sigma$ since we have two compact continuous-symmetry directions (5). All state-space points on a group orbit have the same physical properties, such as kinetic energy, dissipation, or wall friction, since these quantities are invariants of symmetry transformations. In addition, the dynamics of each point on a group orbit can be obtained from the dynamics of a single point following the definition (10) of equivariance. In other words, the state space of pipe flow exhibits much redundancy since a generic point has infinitely many symmetry copies. Moreover, the presence of continuous symmetries renders the study of state space extremely hard: In the presence of the pipe flow's symmetries, measuring the distance between two generic state-space points becomes a question of the minimum distance between tori, whose computational cost can easily become prohibitive if it is to be carried out repeatedly. Continuous-symmetry reduction, which we introduce next, is a coordinate transformation such that state-space points that are related by a continuous symmetry are represented by a single point in the reduced state space.

We begin by reducing the streamwise translation symmetry following [20] exactly: We define a slice template $\hat{a}'$ with a corresponding three-dimensional velocity field, whose each component $\hat{\mathbf{u}}'_k$ is defined as

$$\hat{\mathbf{u}}'_k(z,\theta,r) = J_0(\alpha r)\cos(2\pi z/L), \quad k = 1,2,3, \tag{13}$$

where $J_0$ is the Bessel function of the first kind, which vanishes at the pipe wall, i.e., $J_0(\alpha/2) = 0$. Then the translation symmetry-reduced coordinates are given by

$$\hat{a}(\tau) = g_z(L\phi_z/2\pi)a(\tau), \tag{14}$$

where

$$\phi_z(\tau) = \arg[\langle a(\tau),\hat{a}'\rangle + i\langle a(\tau),g_z(-L/4)\hat{a}'\rangle]. \tag{15}$$

The transformation (14) exists as long as the phase (15) does. Note that $\phi_z$ is the polar angle when the state $a(\tau)$ is projected onto the plane spanned by $(\hat{a}',g_z(-L/4)\hat{a}')$.

Extension of (14) for the azimuthal symmetry reduction is straightforward with a second slice template $\tilde{a}'$ corresponding to the velocity field with components

$$\tilde{\mathbf{u}}'_k(z,\theta,r) = J_0(\alpha r)\cos(\theta), \quad k = 1,2,3. \tag{16}$$

Then the symmetry-reducing coordinate transformation becomes

$$\tilde{a}(\tau) = g_\theta(\phi_\theta)a(\tau), \tag{17}$$

where

$$\phi_\theta(\tau) = \arg[\langle \hat{a}(\tau),\tilde{a}'\rangle + i\langle \hat{a}(\tau),g_\theta(-\pi/2)\tilde{a}'\rangle]. \tag{18}$$

Similar to (14) and (15), the transformation (17) exists as long as the phase (18) does. Our choice of the order at which the continuous symmetries are reduced is merely a convention since the inner products in (15) and (18) remain unchanged under transformations (17) and (14), respectively. This is a result of our particular choice of the slice templates (13) and (16), which do not depend on $\theta$ and $z$, respectively, and the fact that the axial translation and the azimuthal rotation symmetries commute. For a general symmetry group with noncommuting elements, a more careful treatment would have been required.

The slice templates (13) and (16) need not be valid (smooth, divergence-free) pipe flow velocity fields. The only requirement on the slice templates $\hat{a}'$ and $\tilde{a}'$ is that the projections of the 2-torus

$\{g_\theta(\phi)g_z(l)a \mid l \in [0,L), \phi \in [0,2\pi)\}$ onto the $(\hat{a}', g_z(-L/4)\hat{a}')$ and $(\tilde{a}', g_\theta(-\pi/2)\tilde{a}')$ planes must be circles for a generic state $a$. The cosine dependence of (13) and (16) on the respective symmetry directions provides this as long as the projection is nonzero. We determine the rest of the slice templates by experimentation in order to reduce the probability of having a vanishing projection: We decided to use all three velocity components for the template fields in order to receive contributions from all directions. The radial dependence on $J_0(\alpha r)$, on the other hand, is arbitrary and it is conceivable that there could be other equally valid choices. As we will further argue after introducing the slice phase velocities (25), our experience with the slice templates (13) and (16) has been that the symmetry-reduction procedure that we described yields no discontinuities when applied to the generic turbulent trajectories.

Budanur *et al.* [25] showed for a one-dimensional partial differential equation with SO(2) symmetry that polar coordinate transformations similar to (14) and (17) can be reformulated as a slice hyperplane. A slice hyperplane is a set of points perpendicular to the group orbit of a slice template and is transversally intersected by the group orbits of the state-space points in a closed neighborhood of the template. While a general slice has a finite region of applicability, if the template is chosen such that its dependence on the symmetry coordinate depends only on the first Fourier mode, then the slice works for a semi-infinite domain (half hyperplane) that covers all state space of interest, with a regularizable singularity in time. This method is named the first Fourier mode slice in [25] and we refer the reader to [26] for a pedagogical introduction to it.

Reduced coordinates (14) satisfy the half-hyperplane equation

$$\langle \hat{a} - \hat{a}', t_z' \rangle, \quad \langle t_z(\hat{a}), t_z' \rangle > 0, \tag{19}$$

where $t_z(a) = T_z a$ is the group tangent of a state-space point $a$ and $t_z' = t_z(\hat{a}')$. Similarly, we can express the consequent transformation (17) as another half hyperplane in the streamwise symmetry-reduced state space as

$$\langle \tilde{a} - \tilde{a}', t_\theta' \rangle, \quad \langle t_\theta(\tilde{a}), t_\theta' \rangle > 0, \tag{20}$$

where similarly $t_\theta(\hat{a}) = T_\theta(\hat{a})$ and $t_\theta' = t_\theta(\tilde{a}')$.

The main advantage of the reformulations (19) and (20) is that from this perspective one is able to derive projection operators for transforming the tangent space of $a$ to the slice. Letting $\delta a$ be a small perturbation to $a$ in the full state space and $\phi_z$ be the slice phase that transforms $a$ to the slice as $\hat{a} = g_z(\phi_z L/2\pi)a$, then the small perturbation can be transformed to the slice by the projection

$$\delta\hat{a} = \left(1 - \frac{t_z(\hat{a}) \otimes t_z'}{\langle t_z(\hat{a}), t_z' \rangle}\right) g_z(\phi_z L/2\pi)\delta a. \tag{21}$$

Similarly, $\delta\hat{a}$ is transformed to the second slice (20) as

$$\delta\tilde{a} = \left(1 - \frac{t_\theta(\tilde{a}) \otimes t_\theta'}{\langle t_\theta(\tilde{a}), t_\theta' \rangle}\right) g_\theta(\phi_\theta)\delta\hat{a}, \tag{22}$$

where $\phi_\theta$ is the slice-fixing phase (18), i.e., $\tilde{a} = g_\theta(\phi_\theta)\hat{a}$. For the derivation of these projection operators, we refer the reader to the Appendix of [20].

We finish this section by explaining possible shortcomings of the presented symmetry-reduction scheme: With the aid of the projections (21) and (22), it is straightforward to express the state-space velocity in the reduced state space. Replacing $\delta a$ with $v(a)$ in (21), we obtain

$$\hat{v}(\hat{a}) = \left(1 - \frac{t_z(\hat{a}) \otimes t_z'}{\langle t_z(\hat{a}), t_z' \rangle}\right) g_z(\phi_z L/2\pi)v(a),$$

$$\hat{v}(\hat{a}) = v(a) - \frac{\langle t_z', v(\hat{a}) \rangle}{\langle t_z(\hat{a}), t_z' \rangle} t_z(\hat{a}), \tag{23}$$

where we used the first equivariance property in (10) and defined the streamwise symmetry-reduced state-space velocity as $\hat{v}(\hat{a}) = \dot{\hat{a}}$. The fully symmetry-reduced state-space velocity $\tilde{v}(\tilde{a}) = \dot{\tilde{a}}$ can be
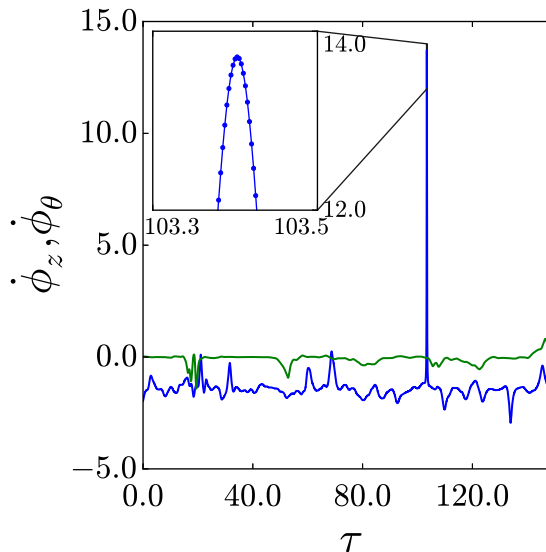
FIG. 2. Phase velocities (25) $\dot{\phi}_z$ (blue) and $\dot{\phi}_\theta$ (green) measured in a typical turbulence simulation. The inset shows a zoom into the time interval $\tau \in [103.3, 103.5]$, where a sharp increase in $\dot{\phi}_z$ is apparent. Dots in the inset correspond to adjacent time steps of the simulation, showing that this episode is in fact time resolved.

similarly written as

$$\tilde{v}(\tilde{a}) = \hat{v}(\tilde{a}) - \frac{\langle t'_\theta, \hat{v}(\tilde{a}) \rangle}{\langle t_\theta(\tilde{a}), t'_\theta \rangle} t_\theta(\tilde{a}). \tag{24}$$

It is instructive to have a close look at (23): The reduced state-space velocity $\hat{v}$ is generated from the full state-space velocity $v$ by subtracting the component in the direction of the group tangent with a prefactor proportional to $v$'s projection onto the slice tangent. The second thing to recognize in (23) is the fact that $\langle t_z(\hat{a}), t'_z \rangle$ appears in the denominator; hence, if this inner product vanishes, the reduced state-space velocity field diverges. For a general slice, this condition sets the border in which the slice may apply [27,28]; in our particular case of the first Fourier mode slice, this condition is equivalent to the existence of the phase (15). It can be shown [29] that the multipliers of group tangents in (23) and (24) correspond to the time derivatives of the parameters of group actions that transform trajectories to the slice, i.e.,

$$\dot{\phi}_z = \left( \frac{2\pi}{L} \right) \frac{\langle t'_z, v(\hat{a}) \rangle}{\langle t_z(\hat{a}), t'_z \rangle}, \quad \dot{\phi}_\theta = \frac{\langle t'_\theta, \hat{v}(\tilde{a}) \rangle}{\langle t_\theta(\tilde{a}), t'_\theta \rangle}. \tag{25}$$

Hence, these are appropriate quantities for checking whether or not the sliced dynamics is within its borders. Our experience with the first Fourier mode slices has been such that these quantities do not diverge for generic trajectories, although they may have "fast" episodes. We illustrate this for a typical turbulent trajectory in Fig. 2. Fast fluctuations that are caused by such episodes can be handled by rescaling the time step of the numerical simulation or the problem can be explicitly reformulated using a slice time [25]. In this study, we found a fixed time step $\Delta\tau = 0.0025$ to be sufficient to resolve the changes in slice phases, without resorting to an adaptive time-stepping scheme.

## III. TRAVELING WAVES ON THE LAMINAR-TURBULENT BOUNDARY

Other than the laminar equilibrium, all invariant solutions such as traveling waves, rotating waves, relative periodic orbits, and possibly higher-dimensional invariant tori of pipe flow drift downstream.

A traveling wave $a_{\mathrm{TW}}$ is the simplest among those, which satisfies

$$a_{\mathrm{TW}}(\tau) = g_z(c\tau)a_{\mathrm{TW}}(0), \tag{26}$$

namely, its sole dynamics is a drift in the axial direction with constant phase speed $c$. Linear stability of this solution is described by the eigenvalue problem [15,30]

$$\left(\left.\frac{dv(a)}{da}\right|_{a=a_{\mathrm{TW}}} - cT_z\right)V_i^{\mathrm{TW}} = \lambda_i^{\mathrm{TW}}V_i^{\mathrm{TW}}, \tag{27}$$

where $\lambda_i^{\mathrm{TW}}$ and $V_i^{\mathrm{TW}}$ are the linear stability eigenvalues and eigenvectors, respectively. Since the state space is formally infinite dimensional, each traveling wave has infinitely many stability eigenvalues and eigenvectors. In practice, we solve (27) by Arnoldi iteration and approximate the finite-dimensional leading (most unstable) part of the tangent space.

Traveling waves become equilibria when the axial translation symmetry is reduced, say, by the first Fourier mode slice method of (14). The translation symmetry-reduced state space still exhibits the $O(2)_\theta$ symmetry and it follows from the normal form analysis that all equilibria of an $O(2)$-equivariant system belong to invariant subspaces of reflection symmetry or its conjugates [31]. Returning to full state space, this implies that all traveling waves of the pipe flow must be invariant under the reflection $\sigma$ or a related symmetry. In particular, the solutions we investigate in what follows are invariant under so-called shift-and-reflect symmetry

$$S = \sigma g_z(L/2) \in G. \tag{28}$$

In the shift-and-reflect subspace, continuous-rotation symmetry (3) of the pipe flow is broken and only the discrete rotation by $\pi$ is allowed [23]. Thus, the symmetry group of shift-and-reflect subspace is

$$G_S = \{g_z(l), g_\theta(\pi)\}. \tag{29}$$

Note that, by definition, reflection symmetry is equivalent to an axial translation by $L/2$.

### A. Unstable manifold of S1

Numerical [6] and experimental [32] (combined with numerical work) evidence strongly suggests that the edge state of axially periodic pipe flow that is not long enough to exhibit streamwise localization is organized around the asymmetric traveling-wave solution found in [3]. Following [4], we refer to this solution as S1. This naming refers to the solution's symmetries: S stands for shift-and-reflect (28) invariance and 1 is the fundamental azimuthal wave number. S1 appears at a low Re through a symmetry-breaking bifurcation of a $g_\theta(\pi)g_z(L/2)$-symmetric solution, which itself is borne out of a saddle-node bifurcation at even lower Re [3]. For the parameters studied here (Re = 3000 and $L = \pi/0.625 \approx 5$) S1 and its two purely real unstable eigenvectors with corresponding eigenvalues $\lambda_1^{S1} = 0.0793$ and $\lambda_2^{S1} = 0.0223$ are visualized in Fig. 3. In Fig. 3(a) and throughout the three-dimensional visualizations of this paper, streamwise velocity isosurfaces are chosen as 75% of their maximum and minimum values for velocity fluctuations. Similarly, vorticity isosurface levels are chosen at 60% of their respective maxima and minima. Numerical values of velocity and vorticity isosurfaces are given in the figure caption. For the two-dimensional cross-sectional visualizations of shift-and-reflect-symmetric states, we chose to average quantities over the first half pipe length since the second half is simply the reflection of the first.

In Fig. 3, besides the eigenvectors $V_{1,2}^{S1}$ [Figs. 3(c) and 3(e)], which are computed in the full state space, we also show $\hat{V}_{1,2}^{S1}$ [Figs. 3(d) and 3(f)], which are obtained by the projection (21). With these visualizations, we would like to emphasize that the symmetry-reduced eigenvector might be quite different from the one that is computed in the full state space, as it is the case for $V_2^{S1}$ [Fig. 3(e)] and $\hat{V}_2^{S1}$ [Fig. 3(f)]. Moreover, it should be understood that the unstable manifold of S1 in the full state space is three dimensional and its linear part is contained within the tangent space spanned by $V_1^{S1}$,
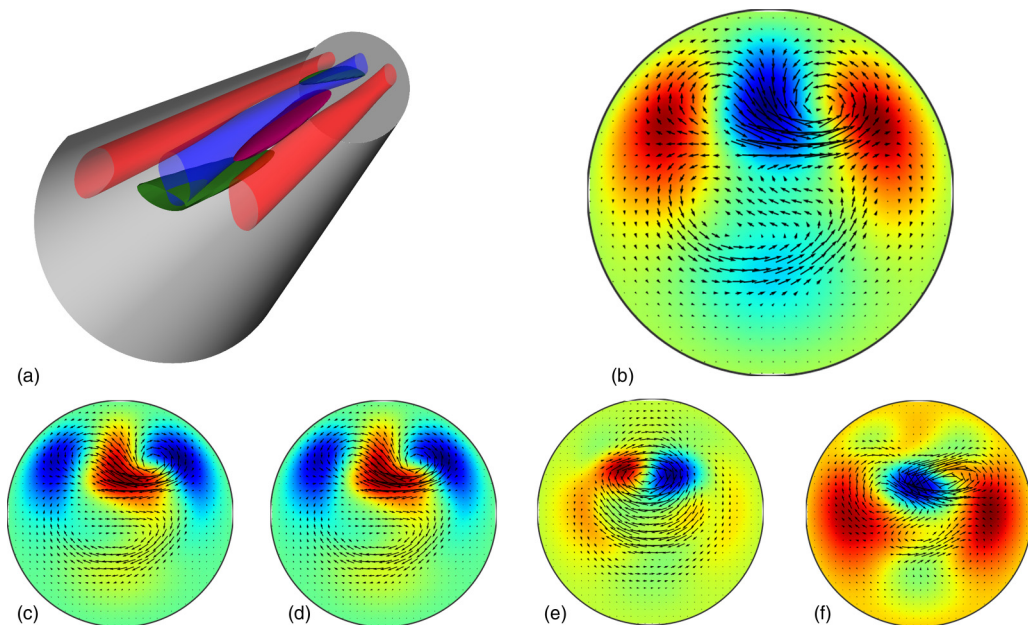
FIG. 3. (a) Isosurfaces of streamwise velocity at $u = 0.26$ (red) and $u = -0.33$ (blue) and streamwise vorticity at $\omega_z = \pm 0.40$ (green and purple, respectively) for the traveling wave S1 in three dimensions. Also shown are the color-coded streamwise velocity and cross-stream velocity (arrows) averaged over (b) the half pipe length $z \in (0, L/2)$ for S1 and the unstable eigenvectors (c) $V_1^{S1}$, (d) $\hat{V}_1^{S1}$, (e) $V_2^{S1}$, and (f) $\hat{V}_2^{S1}$. The flow direction is into the page.

$V_2^{S1}$, and the marginal direction $V_3^{S1} = t_z(a_{S1}) = T_z a_{S1}$ with the eigenvalue $\lambda_3^{S1} = 0$. Note that the projection (21) subtracts components in this direction and its action on $t_z(a_{S1})$ yields a zero vector. In other words, the marginal stability direction, which corresponds to axial drift of the traveling wave, is eliminated by slicing. Thus, within the slice, S1 has a two-dimensional unstable manifold, whose linear part is contained in the $(\hat{V}_1^{S1}, \hat{V}_2^{S1})$ plane.

Duguet *et al.* [6] studied the evolution of perturbations along the unstable directions of S1. After confirming that the perturbations in the $\pm V_1^{S1}$ direction either laminarizes or develops into turbulence, they focused on the perturbations on the $(V_1^{S1}, V_2^{S1})$ plane that neither laminarize nor become turbulent. Running Newton searches near recurrences of these trajectories, they found a rotated version of S1 and conjectured that S1's unstable manifold contains a "relative" heteroclinic connection to its rotation by approximately $52°$. This cannot be true since the unstable eigenvectors $V_1^{S1}$ and $V_2^{S1}$ are also shift-and-reflect symmetric, hence the associated unstable manifold lies in the shift-and-reflect invariant subspace, which only allows for azimuthal rotations by $\pi$. We are guessing that the Duguet *et al.* conjecture was a result of a numerical error buildup due to not restricting dynamics in the shift-and-reflect invariant subspace. Our first calculation in this paper will be very similar to theirs, with the symmetry-restriction requirement taken into account. In addition, we carry out our computation in the translation symmetry-reduced state space (14), which allows us to visualize the unstable manifold.

As a first approximation to S1's unstable manifold, we start trajectories with the initial conditions

$$\hat{a}_\phi(\tau = 0) = \hat{a}_{S1} + \epsilon \left( \frac{\hat{V}_1^{S1}}{\lambda_1^{S1}} \cos \phi + \frac{\hat{V}_2^{S1}}{\lambda_2^{S1}} \sin \phi \right), \tag{30}$$

where $\hat{a}_{S1}$ is the symmetry-reduced state-space point corresponding to S1, $\hat{V}_1^{S1}$ and $\hat{V}_2^{S1}$ are S1's leading linear stability eigenvectors projected onto the slice as described in (21), and $\epsilon = 10^{-4}$ is a
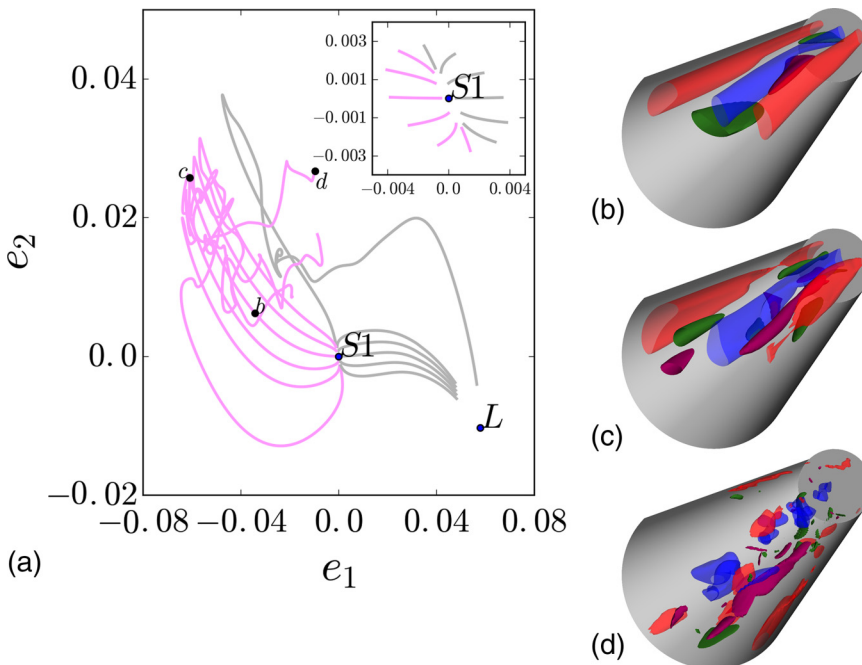
FIG. 4. (a) First approximation to the unstable manifold of S1, as forward-integrated trajectories with initial conditions (30) visualized as projections onto the local coordinate frame (31). Here $L$ denotes the laminar solution. The inset shows the same 12 trajectories on the unstable manifold for the time interval $\tau \in [0,2.5]$, illustrating the initial almost uniform expansion. Isosurfaces of streamwise velocity and vorticity at (b) $u = 0.36$ (red), $u = -0.50$ (blue), and $\omega_z = \pm 0.99$ (green and purple, respectively); (c) $u = 0.50$ (red), $u = -0.62$ (blue), and $\omega_z = \pm 1.5$ (green and purple, respectively); and (d) $u = 0.66$ (red), $u = -0.71$ (blue), and $\omega_z = \pm 9.0$ (green and purple, respectively). The flow direction is into the page.

small constant. Equation (30) defines an ellipse on the $(\hat{V}_1^{S1}, \hat{V}_2^{S1})$ hyperplane, parametrized by $\phi$, and the scaling of perturbations by corresponding eigenvalues $\lambda_{1,2}^{S1}$ lets trajectories expand initially at similar rates [33]. This is illustrated in the inset of Fig. 4(a), where $\hat{a}_\phi(\tau)$ for $\tau \in [0,2.5]$ is shown for 12 equally spaced trajectories in $\phi \in [0,2\pi)$ as projections onto the local bases formed by orthogonalizing $\hat{V}_1^{S1}$ and $\hat{V}_2^{S1}$, i.e.,

$$e_1 = \langle \hat{a}_\phi(\tau) - \hat{a}_{S1}, \hat{V}_{1,\perp}^{S1} \rangle, \quad e_2 = \langle \hat{a}_\phi(\tau) - \hat{a}_{S1}, \hat{V}_{2,\perp}^{S1} \rangle. \tag{31}$$

In (31), the subscript $\perp$ indicates that $\hat{V}_1^{S1}$ and $\hat{V}_2^{S1}$ are orthonormalized via the Gram-Schmidt procedure, i.e., $\hat{V}_{2,\perp}^{S1}$ is formed by subtracting $\hat{V}_2^{S1}$'s projection onto the $\hat{V}_1^{S1}$ direction and normalization. The inset of Fig. 4(a) illustrates that these bases capture local dynamics very well. In particular, note that the trajectories starting from the initial conditions (30) with $\phi = k\pi/2$, $k = 0,1,2,3$, are initially straight as they correspond to the perturbations in the symmetry-reduced eigenvector directions, whereas the rest appear bent since the two unstable directions expand at different rates. Figure 4(a) shows these trajectories for longer times, until they either become turbulent or laminarize. The trajectories that become turbulent or relaminarize are respectively colored pink and gray. While the projections are locally reliable, they fail to fully capture the dynamics away from S1 since the trajectories seem to fold onto themselves. In order to illustrate the qualitative features of the transition, we marked three instances on $\hat{a}_\pi(\tau)$ at $\tau \in [40,60,90]$ and visualized the corresponding three-dimensional flow structures [Figs. 4(b)–4(d)]. Note that the structures in Fig. 4(b) are quite similar to those of S1, while the isosurface levels are set to higher values. This illustrates the first part of the transition: As the trajectory moves from S1 towards turbulence,
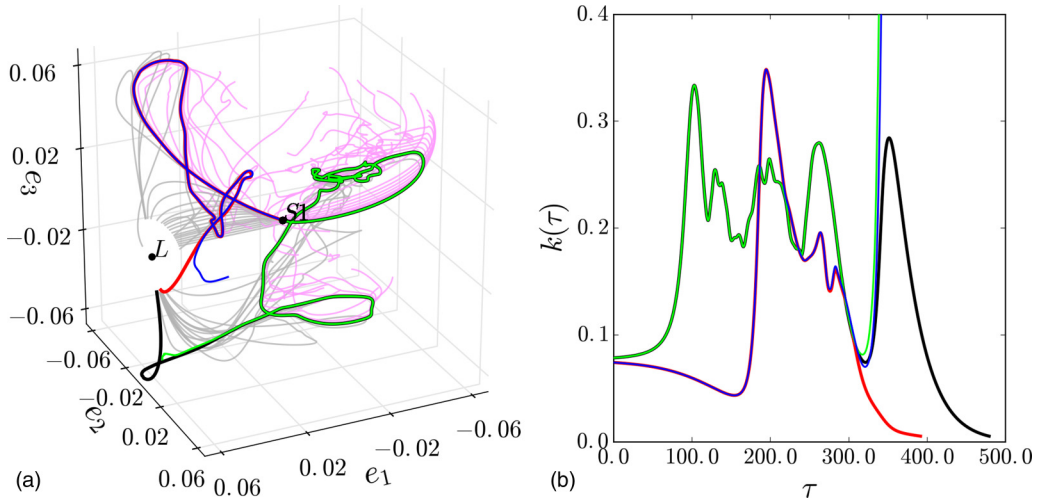
FIG. 5. (a) Unstable manifold of S1 approximated by bisecting between trajectories that relaminarize and those that develop into turbulence. (b) Time series of kinetic energy for trajectories that stay on the edge for the longest times.

streaks and vortices are amplified while their overall shape is more or less unchanged. As can be seen in Fig. 4(c), this initial amplification is followed by the breakdown of streaks, and eventual turbulence [Fig. 4(d)] no longer exhibits structures that are coherent throughout the computational domain.

The 12-trajectory approximation to the two-dimensional unstable manifold is initially successful and illustrates the general features of the unstable manifold such as relaminarization and transition to turbulence. It is clear from Fig. 4(a) that this approximation very quickly fails to cover the extent of the manifold that stays in the laminar-turbulent boundary. In order to uncover details of this part, we bisected between trajectories that transition to turbulence or relaminarize by changing $\phi$ in (30) until reaching the limit of numerical precision, as done in [6]. Differently, however, we enforced shift-and-reflect invariance in the time stepping, in order to avoid numerical errors that could take trajectories outside the invariant subspace. In order to improve visibility, we visualized the unstable manifold approximated this way in three dimensions, using the least contracting stability eigenvector $\hat{V}_{4,\perp}^{S1}$ (symmetry reduced and orthonormalized) in addition to the leading two (31) as the third basis. The unstable manifold visualized this way is shown in Fig. 5(a), where we colored trajectories that eventually laminarize gray and those that transition to turbulence pink. Additionally, we plotted the last four trajectories in the bisection procedure thicker than the rest, using colors red, blue, green, and black. For comparison, the time series of the kinetic energy for these four trajectories is shown in Fig. 5(b), where we see that the trajectories stay on the edge longer than 300 time units.

Upon our investigation of the trajectories that stay on the edge for the longest times, we observed episodes where state-space trajectories slow down, which might indicate visits to the neighborhoods of other traveling waves. In order to quantify this, we measured the self-recurrence, which we defined as the norm of the difference between the symmetry-reduced states at times $\tau$ and $\tau - 5$ on the same trajectory. Note that in the symmetry-reduced state space, the traveling waves are equilibria, thus no extra care for the translation symmetry is necessary. Figure 6 shows the self-recurrence [Fig. 6(a)] over the trajectory which is shown in blue in Fig. 5 and flow structures at different times on this trajectory [Figs. 6(b)–6(e)].

As the trajectory evolves on the edge, it visits states with qualitatively different features: At the first minimum [Fig. 6(c)] of the self-recurrence function, new fast streaks begin to form on the downside
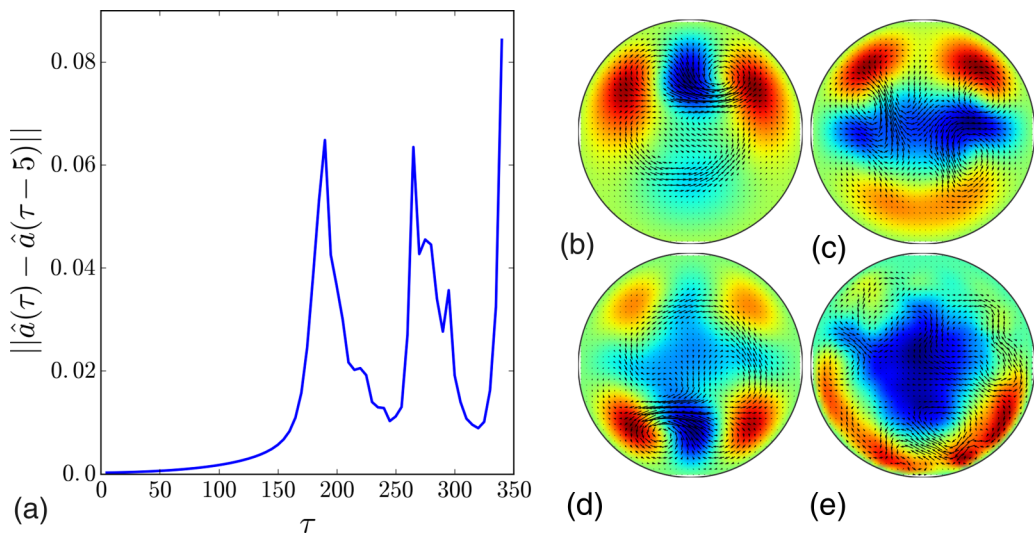
FIG. 6. (a) Self-recurrence measured over an edge trajectory (drawn in blue in Fig. 5) on the unstable manifold of S1. Also shown are the color-coded (fast and slow in red and blue, respectively) streamwise velocity and cross-sectional velocity (arrows) averaged over the half pipe length ($z \in [0, L/2]$) at (b) initial time $\tau = 0$, (c) local minimum $\tau = 245$, (d) local minimum $\tau = 320$, and (e) final time $\tau = 345$. The flow direction is into the page.

of the pipe cross section and at the second minimum [Fig. 6(d)] initial fast streaks begin to disappear. The eventual transition to turbulence [Fig. 5(e)] has quantitative features similar to those illustrated in Fig. 4: Streaks amplify, spread, and break into smaller-scale structures on the opposite side of the pipe. Newton-Krylov-hookstep searches starting from initial conditions visualized in Figs. 6(c) and 6(d) converged to traveling-wave solutions: Starting from the latter, we find S1, rotated by $\pi$ about the pipe axis. In contrast, the Newton search starting from Fig. 6(c) leads us to a different traveling wave, which we study in the next section.
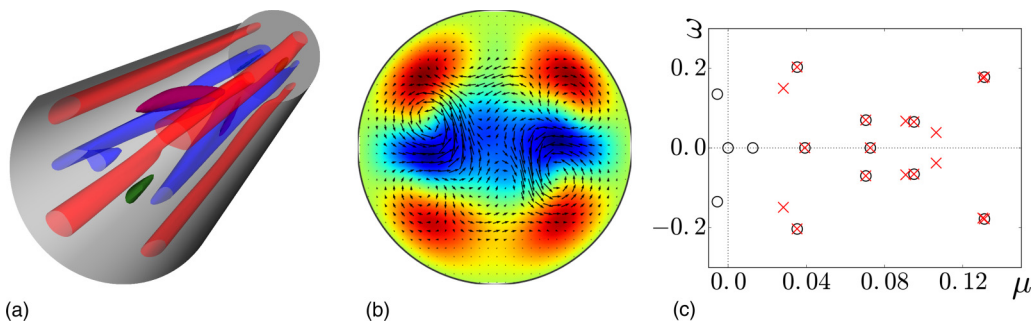


FIG. 7. (a) Isosurfaces of streamwise velocity at $u = 0.27$ and $-0.38$ (red and blue, respectively) and streamwise vorticity at $\omega_z = \pm 0.96$ (green and purple, respectively) of S1N. (b) Color-coded (fast and slow in red and blue, respectively) streamwise velocity and cross-sectional velocity (arrows) averaged over the half pipe length ($z \in [0, L/2]$) visualization of S1N. (c) Leading linear stability eigenvalues of S1N on the complex plane computed in shift-and-reflect invariant subspace (black circles) and full state space (red crosses).
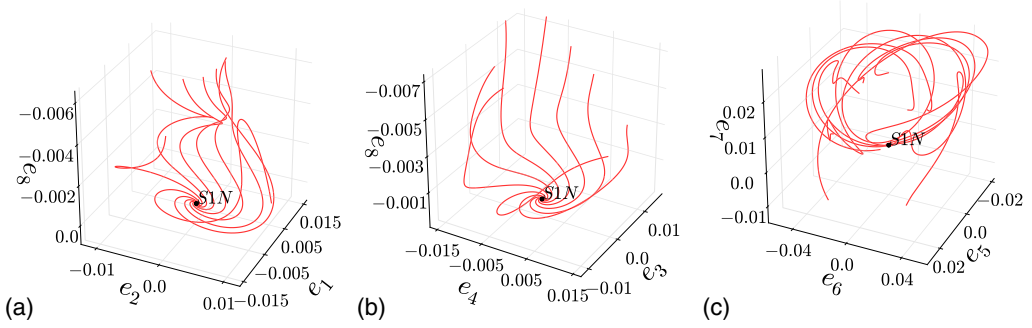
FIG. 8. Two-dimensional surfaces associated with the three leading unstable eigenvectors of S1N approximated as a set of trajectories with initial conditions given by (32) for (a) $k = 1$, (b) $k = 3$, and (c) $k = 5$.

## B. Unstable manifold of S1N

Figures 7(a) and 7(b) show three- and two-dimensional visualizations of our solution, which we hereafter refer to as S1N. While being on the laminar-turbulent boundary, S1N has a much more complicated structure than S1; its kinetic energy is roughly twice that of S1 and it has many more unstable directions. Solutions with similar properties were known [2,4,6,22], mostly with higher azimuthal symmetries. However, the relevance of the previously know solutions to the full problem (without imposed symmetries) was not established. Similarities between the initial condition's [Fig. 6(c)] and the converged state's flow structures [Fig. 7(b)] are apparent. Note particularly the locations of the vortical structures, which align very well. Since these structures do not extend along the pipe axis like streaks do, their one-to-one comparison is made possible by reduction to the translation-reduced state space (14).

As shown in Fig. 7(c), S1N's unstable manifold is 11 dimensional in the shift-and-reflect subspace and more unstable eigenvalues were found when the symmetry restriction was lifted. This renders a complete computational study of its unstable manifold impractical. Therefore, in Fig. 8, we visualize two-dimensional surfaces associated with each of the leading three complex unstable eigenvalues in the full state space as the application of symmetry reduction in both $z$ and $\theta$.

Let $\lambda_k^{\mathrm{S1N}} = \mu_k^{\mathrm{S1N}} + i\omega_k^{\mathrm{S1N}}$ and $V_k^{\mathrm{S1N}} = U_k^{\mathrm{S1N}} + iW_k^{\mathrm{S1N}}$ be complex eigenvalues and eigenvectors of S1N, respectively. The set of trajectories that approximately covers the linearized dynamics in the local two-dimensional plane spanned by $(U_k^{\mathrm{S1N}}, W_k^{\mathrm{S1N}})$ is given by

$$\tilde{a}_\delta(\tau = 0) = \tilde{a}_{\mathrm{S1N}} + \epsilon \exp\left(2\pi \mu_k^{\mathrm{S1N}} \delta / \omega_k^{\mathrm{S1N}}\right) \tilde{U}_k^{\mathrm{S1N}}, \tag{32}$$

where $\delta \in [0,1)$. In (32), $\epsilon$ is a small number and a tilde implies that state-space points and eigenvectors are transformed into the first Fourier mode slice via (17) and (22), respectively. Under the linearized dynamics, a small perturbation to $\tilde{a}_{\mathrm{S1N}}$ in the $\tilde{U}_k$ direction expands by $\exp(2\pi \mu_k^{\mathrm{S1N}} / \omega_k^{\mathrm{S1N}})$ at one return of the spiral. Thus, the trajectories starting from the initial conditions (32) approximately satisfy $\tilde{a}_{\delta=0}(2\pi / \omega_k^{\mathrm{S1N}}) = \tilde{a}_{\delta=1}(0)$, covering the associated two-dimensional (2D) surface. Using this approximation, we visualized the time-forward dynamics of 2D surfaces associated with $V_{1,2}^{\mathrm{S1N}}$, $V_{3,4}^{\mathrm{S1N}}$, and $V_{5,6}^{\mathrm{S1N}}$ in Figs. 8(a)–8(c), respectively. We assume that the eigenvalues are ordered from most unstable to the least, i.e., $\mathrm{Re}\,\lambda_1^{\mathrm{S1N}} \geqslant \mathrm{Re}\,\lambda_2^{\mathrm{S1N}} \geqslant \mathrm{Re}\,\lambda_3^{\mathrm{S1N}} \geqslant \cdots$. Note that complex eigenvalues and eigenvectors satisfy $\lambda_1^{\mathrm{S1N}} = \lambda_2^{\mathrm{S1N}*}, \lambda_3^{\mathrm{S1N}} = \lambda_4^{\mathrm{S1N}*}, \lambda_5^{\mathrm{S1N}} = \lambda_6^{\mathrm{S1N}*}, V_1^{\mathrm{S1N}} = V_2^{\mathrm{S1N}*}, V_3^{\mathrm{S1N}} = V_4^{\mathrm{S1N}*}$, and $V_5^{\mathrm{S1N}} = V_6^{\mathrm{S1N}*}$, where the asterisk stands for complex conjugation. Projection bases $\mathbf{e}_{1,2}$, $\mathbf{e}_{3,4}$, and $\mathbf{e}_{5,6}$ are generated from $\tilde{V}_1^{\mathrm{S1N}}$, $\tilde{V}_3^{\mathrm{S1N}}$, and $\tilde{V}_5^{\mathrm{S1N}}$ as follows. By definition, $\tilde{V}_k^{'\mathrm{S1N}} = e^{i\phi} \tilde{V}_k^{\mathrm{S1N}}$ is a stability eigenvector with eigenvalue $\lambda_k^{\mathrm{S1N}}$. If we choose

$$\phi = \frac{1}{2} \arctan \frac{2\langle \tilde{U}_k^{\mathrm{S1N}}, \tilde{W}_k^{\mathrm{S1N}} \rangle}{\left\| \tilde{W}_k^{\mathrm{S1N}} \right\|^2 - \left\| \tilde{U}_k^{\mathrm{S1N}} \right\|^2}, \tag{33}$$
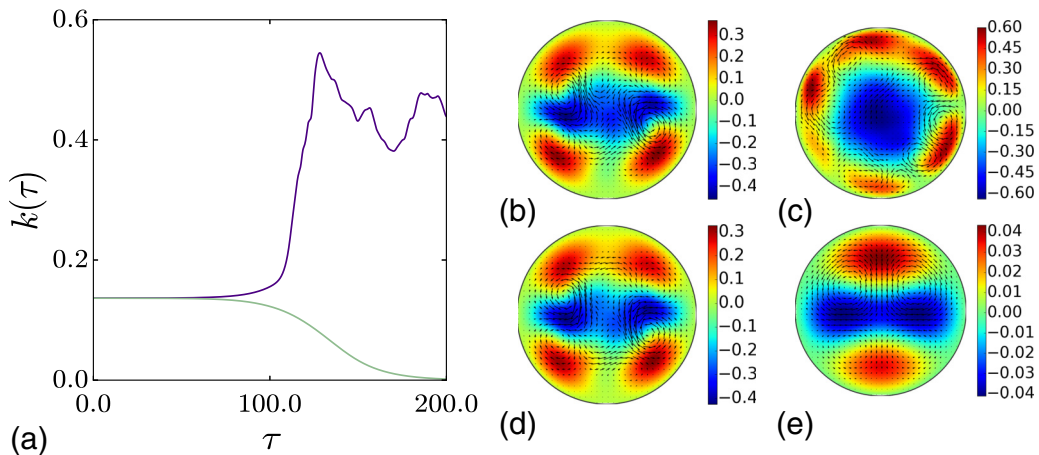
FIG. 9. (a) Time evolution of kinetic energy for trajectories starting from $a_{\text{S1N}} \pm 10^{-4} V_{11}^{\text{S1N}}$ (green and purple, respectively). Also shown are the color-coded streamwise velocity and cross-sectional velocity (arrows) averaged over the half pipe length ($z \in [0, L/2]$) at times (b) and (d) $\tau = 100$ and (c) and (e) $\tau = 200$ for (b) and (c) the transition to turbulence [purple in (a)] and (d) and (e) laminarization [green in (a)].

$\tilde{U}_k^{'\text{S1N}} = \text{Re } \tilde{V}_k^{'\text{S1N}}$ and $\tilde{W}_k^{'\text{S1N}} = \text{Im } \tilde{V}_k^{'\text{S1N}}$ become orthogonal, i.e., $\langle \tilde{U}_k^{'\text{S1N}}, \tilde{W}_k^{'\text{S1N}} \rangle = 0$. Projection bases are formed from these vectors as $(\mathbf{e}_k, \mathbf{e}_{k+1}) = (\tilde{U}_k^{'\text{S1N}}/\|\tilde{U}_k^{'\text{S1N}}\|, \tilde{W}_k^{'\text{S1N}}/\|\tilde{W}_k^{'\text{S1N}}\|)$ for $k = 1, 3, 5$. These bases fully capture local two-dimensional dynamics. We chose the third projection direction by trial and error to capture as much as possible as the trajectories develop into turbulence: $\mathbf{e}_7 = \tilde{V}_{11}^{\text{S1N}}/\|\tilde{V}_{11}^{\text{S1N}}\|$ and $\mathbf{e}_8 = \tilde{V}_1^{\text{S1}}/\|\tilde{V}_1^{\text{S1}}\|$. Here $\tilde{V}_{11}^{\text{S1N}}$ is the real unstable eigenvector of S1N with largest real eigenvalue $\lambda_{11}^{\text{S1N}}$ and $\tilde{V}_1^{\text{S1}}$ is the leading eigenvector of S1. We have already illustrated in Sec. III B that the $V_1^{\text{S1}}$ direction corresponds to the trajectories in the vicinity of S1, which either laminarize or become turbulent, and we are going to demonstrate that $V_{11}^{\text{S1N}}$ takes the same role for S1N.

Openpipeflow normalizes stability eigenvectors such that their norms are equal to that of the associated solution, i.e., $\|V_k^{\text{TW}}\| = \|a_{\text{TW}}\|$. For computations of Fig. 8, we set $\epsilon = 10^{-4}$ [Figs. 8(a) and 8(b)] and $\epsilon = 10^{-8}$ [Fig. 8(c)] and picked eight equidistant point in $[0, 1)$ for $\delta$. While the spiral-out dynamics is clearly visible in Figs. 8(a) and 8(b), trajectories look less organized in Fig. 8(c). This is because the imaginary part of the fifth eigenvalue $\lambda_5^{\text{S1N}} = 0.106 + i0.0383$ is rather small, rendering the time for the trajectories to complete a full spiral long. This is not the case for $\lambda_1^{\text{S1N}} = 0.131 + i0.178$ and $\lambda_3^{\text{S1N}} = 0.130 + i0.176$. While we might have obtained a better representation of the 2D manifold in Fig. 8(c) if we had used more trajectories to represent it, we chose to leave it as it is in order to illustrate the possible shortcomings of the method. All trajectories in Fig. 8 eventually become turbulent, illustrating the rich dynamics that the laminar-turbulent boundary can exhibit.

In the full state space, the leading ten stability eigenvalues of S1N are complex conjugate [Fig. 7(c)] and $\lambda_{11}^{\text{S1N}} = 0.0727$ is purely real. In Fig. 9(a), we show the time evolution of the kinetic energy when S1N is perturbed in the $\pm V_{11}^{\text{S1N}}$ direction. As one would expect from a solution on the laminar-turbulent boundary, the flow relaminarizes in one direction while becoming turbulent in the opposite. While this observation clearly shows that S1N also belongs to the laminar-turbulent boundary, whether or not its presence influences generic edge trajectories is not known. In the next section, we investigate this through a numerical experiment.

## C. Approaches to the traveling waves

In order to illustrate how a generic trajectory on the laminar-turbulent boundary is influenced by the traveling-wave solutions present in the edge state, we carried out an edge tracking [9,34] experiment
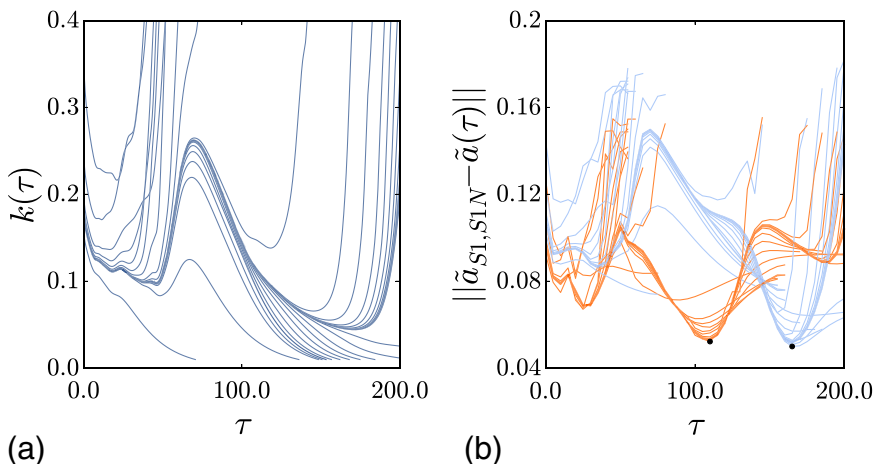
FIG. 10. (a) Time evolution of turbulent kinetic energy for edge tracking trajectories obtained through bisection. (b) Distance of bisection trajectories from S1 (blue) and S1N (orange). Minima of distances at $\tau = 110$ [min $\|\tilde{a}_{S1N} - \tilde{a}(\tau)\|$] and at $\tau = 165$ [min $\|\tilde{a}_{S1} - \tilde{a}(\tau)\|$] are marked black.

where we bisected between initial conditions that become turbulent and those that laminarize. For this purpose, we randomly took a typical turbulent state at Re = 10 000, scaled this field down by constants $c = 0.5$ and $c = 0.75$, and used these states as initial conditions at Re = 3000. After observing that the former uneventfully proceeds towards the laminar solution while the latter triggers turbulence, we began generating new initial conditions by bisecting in $c$ until we reached the limit of our numerical precision such that the resulting trajectories stay in the laminar-turbulent boundary for longer and longer times. Kinetic energy time series of these trajectories are shown in Fig. 10(a). Such initial conditions are expected to approach the invariant edge state [5] irrespective of how the very first state is generated. Therefore, our choice of initial state from Re = 10 000 is arbitrary and many other initial states would approach the edge state following the same algorithm.

For every trajectory we generated through edge tracking we sampled flow states at intervals of $\Delta\tau = 5$ and transformed these states to the first Fourier mode slice through (17). We then measured the distances of these states from S1 and S1N within the first Fourier mode slice. The $L_2$ distances of edge tracking trajectories from S1 and S1N are shown in blue and orange, respectively, in Fig. 10(b), where each set of curves has a clear minimum marked with a black dot. We visualized these closest approaches next to the traveling waves they approach in Fig. 11. Similarities between the flow structures of the traveling waves and the edge trajectories near them are clear, although the correspondence is not one to one.
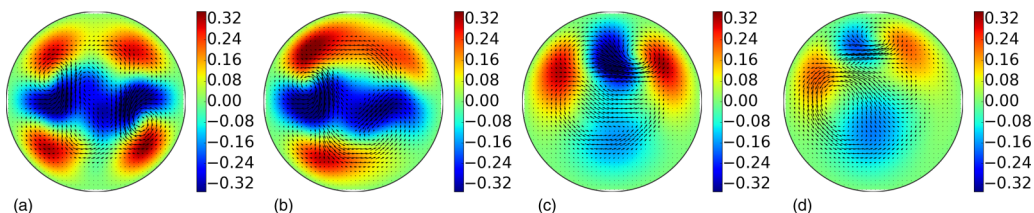


FIG. 11. Color-coded streamwise velocity and cross-sectional velocity (arrows) averaged over the half pipe length ($z \in [0, L/2]$) of (a) S1N, (b) closest approach of the trajectory on the edge to S1N at $\tau = 110$, (c) S1, and (d) closest approach of the trajectory on the edge to S1 at $\tau = 165$. Each figure uses a fixed color scale (min , max) = $(-0.35, 0.35)$.

Notice that without the symmetry reduction, such an analysis would have required an optimization over axial translations and azimuthal rotations for each step in order to minimize the distance between two states. Symmetry reduction eliminates this step, decreasing the computational cost of the analysis tremendously.

## IV. CONCLUSION AND OUTLOOK

In this paper, we introduced a representation of the pipe flow where the continuous symmetries in the axial and azimuthal directions are simultaneously reduced. This technical step was a straightforward extension of the first Fourier mode slice implementation of Ref. [20]. Nevertheless, it was not implemented therein and it successfully closes the continuous-symmetry reduction problem for pipe flow. Adapting this method to other canonical shear flows is straightforward. For instance, in a channel geometry, the role of axial and azimuthal coordinates is taken over by streamwise and spanwise coordinates and one should only make a choice for the wall-normal dependence of the template functions. Since this choice is somewhat arbitrary, a convenient option could be the first Chebyshev polynomial that is often used for numerical discretization in this direction.

For the application, we decided to revisit the laminar-turbulent boundary in a short ($L \approx 5$) periodic computational cell of the pipe flow. Our first calculation that approximated the unstable manifold of S1 was very similar to that of Duguet *et al.* [6], who conjectured that the unstable manifold of S1 reached the neighborhoods of its own azimuthally rotated copies when it is followed along the laminar-turbulent boundary. Differently from Ref. [6], we restricted our computation of the unstable manifold into the shift-and-reflect invariant subspace, to which the unstable manifold belongs. In addition, we visualized the unstable manifold as low-dimensional projections from the first Fourier mode slice (14). We found numerical evidence that the portion of this unstable manifold that is confined in the laminar-turbulent boundary visits the neighborhood of a different traveling wave, which we named S1N. The linear stability spectrum in Fig. 7(c) showed that S1N has a very-high-dimensional unstable manifold, albeit on the laminar-turbulent boundary. By visualizing two-dimensional surfaces associated with leading three complex conjugate unstable eigenvectors in Fig. 7, we illustrated a variety of paths from the edge state leading to the turbulence. Besides demonstrating the utility of the symmetry reduction in both $z$ and $\theta$, this computation also shows how rich the dynamics on the laminar-turbulent boundary can be. One main message we would like to deliver with the aid of these illustrations is that the asymptotic dynamics on the laminar-turbulent boundary in pipe flow should not be treated as a single state; instead, the edge state contains different regions with qualitatively different dynamics dictated by the nearby invariant solutions.

Both traveling waves we studied in this paper belonged to the shift-and-reflect invariant subspace of the pipe flow. One might argue against their relevance for the dynamics in the laminar-turbulent boundary since generic trajectories exist in the full state space. Cvitanović *et al.* [35] nicely illustrated for the one-dimensional Kuramoto-Sivashinsky system that the unstable manifolds of equilibrium solutions, all of which belong to the reflection invariant subspace, successfully capture the qualitative dynamics in the full state space of the O(2)-equivariant system. Our case here is similar to theirs since the symmetry in the azimuthal direction is also O(2). Therefore, it is quite reasonable to expect for S1's unstable manifold to form the backbone of the asymptotic dynamics on the laminar-turbulent boundary, given all the evidence that the edge state is located in its vicinity. Indeed, visualizations of Fig. 11 clearly show the similarities between the full state-space trajectories and the traveling waves nearby.

Recently, Suri *et al.* [36] studied the weakly turbulent quasi-two-dimensional flow experimentally and numerically. They demonstrated that when a turbulent trajectory comes close to an equilibrium, it leaves this neighborhood by following the unstable manifold of the solution. The tools we presented here, in particular, the methods for approximating and visualizing the unstable manifolds after symmetry reduction, pave the way for a similar analysis in three-dimensional pressure-driven flows, which have traveling-wave solutions rather than equilibria.

As we have shown in Sec. III C, symmetry reduction frees us from reduced metrics, such as energy input or dissipation, that do not carry all information of the state spaceand allows for measuring distances in the full state space. However, one should always keep in mind that two points that are at a short distance in the state space of a nonlinear system might evolve towards completely different regions. In order to conclusively answer whether or not a state-space trajectory is "guided" by a particular unstable manifold, we should measure distances between curves in the state space, rather than points. While the finite-dimensional projections such as Figs. 4, 5, and 8 serve this purpose, they do not provide a complete picture of the infinite-dimensional state space. We believe developing computationally feasible methods for comparing shapes in high-dimensional state spaces is an important future problem for turbulence studies.

[1] A. Meseguer and L. N. Trefethen, Linearized pipe flow to Reynolds number $10^7$, J. Comput. Phys. **186**, 178 (2003).

[2] H. Faisst and B. Eckhardt, Traveling Waves in Pipe Flow, Phys. Rev. Lett. **91**, 224502 (2003).

[3] C. C. T. Pringle and R. R. Kerswell, Asymmetric, Helical, and Mirror-Symmetric Traveling Waves in Pipe Flow, Phys. Rev. Lett. **99**, 074502 (2007).

[4] C. C. T. Pringle, Y. Duguet, and R. R. Kerswell, Highly symmetric traveling waves in pipe flow, Philos. Trans. R. Soc. A **367**, 457 (2009).

[5] T. M. Schneider, B. Eckhardt, and J. A. Yorke, Turbulence, Transition, and the Edge of Chaos in Pipe Flow, Phys. Rev. Lett. **99**, 034502 (2007).

[6] Y. Duguet, A. P. Willis, and R. R. Kerswell, Transition in pipe flow: The saddle structure on the boundary of turbulence, J. Fluid Mech. **613**, 255 (2008).

[7] F. Mellibovsky, A. Meseguer, T. M. Schneider, and B. Eckhardt, Transition in Localized Pipe Flow Turbulence, Phys. Rev. Lett. **103**, 054502 (2009).

[8] E. Hopf, A mathematical example displaying features of turbulence, Commun. Pure Appl. Math. **1**, 303 (1948).

[9] T. Itano and S. Toh, The dynamics of bursting process in wall turbulence, J. Phys. Soc. Jpn. **70**, 703 (2001).

[10] S. Toh and T. Itano, A periodic-like solution in channel flow, J. Fluid Mech. **481**, 67 (2003).

[11] T. M. Schneider, J. F. Gibson, M. Lagha, F. De Lillo, and B. Eckhardt, Laminar-turbulent boundary in plane Couette flow, Phys. Rev. E **78**, 037301 (2008).

[12] T. M. Schneider, D. Marinc, and B. Eckhardt, Localized edge states nucleate turbulence in extended plane Couette cells, J. Fluid Mech. **646**, 441 (2010).

[13] S. Zammert and B. Eckhardt, A spotlike edge state in plane Poiseuille flow, PAMM **14**, 591 (2014).

[14] T. Khapko, T. Kreilos, P. Schlatter, Y. Duguet, B. Eckhardt, and D. S. Henningson, Edge states as mediators of bypass transition in boundary-layer flows, J. Fluid Mech. **801**, R2 (2016).

[15] P. Cvitanović, R. Artuso, R. Mainieri, G. Tanner, and G. Vattay, *Chaos: Classical and Quantum* (Niels Bohr Institute, Copenhagen, 2015), available at http://www.ChaosBook.org

[16] G. Kawahara and S. Kida, Periodic motion embedded in plane Couette turbulence: Regeneration cycle and burst, J. Fluid Mech. **449**, 291 (2001).

[17] D. Viswanath, Recurrent motions within plane Couette turbulence, J. Fluid Mech. **580**, 339 (2007).

[18] P. Ritter, F. Mellibovsky, and M. Avila, Emergence of spatio-temporal dynamics from exact coherent solutions in pipe flow, New J. Phys. **18**, 083031 (2016).

[19] J. F. Gibson, J. Halcrow, and P. Cvitanović, Visualizing the geometry of state space in plane Couette flow, J. Fluid Mech. **611**, 107 (2008).

[20] N. B. Budanur and B. Hof, Heteroclinic path to spatially localized chaos in pipe flow, J. Fluid Mech. **827**, R1 (2017).

[21] A. P. Willis, The Openpipeflow Navier-Stokes solver, Software X **6**, 124 (2017).

[22] H. Wedin and R. R. Kerswell, Exact coherent structures in pipe flow: Traveling wave solutions, J. Fluid Mech. **508**, 333 (2004).

[23] N. B. Budanur, K. Y. Short, M. Farazmand, A. P. Willis, and P. Cvitanović, Relative periodic orbits form the backbone of turbulent pipe flow, J. Fluid Mech. **833**, 274 (2017).

[24] A. P. Willis, P. Cvitanović, and M. Avila, Revealing the state space of turbulent pipe flow by symmetry reduction, J. Fluid Mech. **721**, 514 (2013).

[25] N. B. Budanur, P. Cvitanović, R. L. Davidchack, and E. Siminos, Reduction of the SO(2) Symmetry for Spatially Extended Dynamical Systems, Phys. Rev. Lett. **114**, 084102 (2015).

[26] N. B. Budanur, D. Borrero-Echeverry, and P. Cvitanović, Periodic orbit analysis of a system with continuous symmetry–A tutorial, Chaos **25**, 073112 (2015).

[27] S. Froehlich and P. Cvitanović, Reduction of continuous symmetries of chaotic flows by the method of slices, Commun. Nonlinear Sci. Numer. Simul. **17**, 2074 (2012).

[28] P. Cvitanović, D. Borrero-Echeverry, K. Carroll, B. Robbins, and E. Siminos, Cartography of high-dimensional flows: A visual guide to sections and slices, Chaos **22**, 047506 (2012).

[29] C. W. Rowley and J. E. Marsden, Reconstruction equations and the Karhunen-Loéve expansion for systems with symmetry, Physica D **142**, 1 (2000).

[30] P. Chossat and R. Lauterbach, *Methods in Equivariant Bifurcations and Dynamical Systems* (World Scientific, Singapore, 2000).

[31] D. Armbruster, J. Guckenheimer, and P. Holmes, Heteroclinic cycles and modulated traveling waves in systems with O(2) symmetry, Physica D **29**, 257 (1988).

[32] A. de Lozar, F. Mellibovsky, M. Avila, and B. Hof, Edge State in Pipe Flow Experiments, Phys. Rev. Lett. **108**, 214502 (2012).

[33] B. Krauskopf, H. M. Osinga, E. J. Doedel, M. E. Henderson, J. Guckenheimer, A. Vladimirsky, M. Dellnitz, and O. Junge, A survey of methods for computing (un)stable manifolds of vector fields, Int. J. Bifurcat. Chaos **15**, 763 (2005).

[34] J. D. Skufca, J. A. Yorke, and B. Eckhardt, Edge of Chaos in a Parallel Shear Flow, Phys. Rev. Lett. **96**, 174101 (2006).

[35] P. Cvitanović, R. L. Davidchack, and E. Siminos, On the state space geometry of the Kuramoto-Sivashinsky flow in a periodic domain, SIAM J. Appl. Dyn. Syst. **9**, 1 (2009).

[36] B. Suri, J. Tithof, R. O. Grigoriev, and M. F. Schatz, Forecasting Fluid Flows using the Geometry of Turbulence, Phys. Rev. Lett. **118**, 114501 (2017).